

Trajectory Vorticity - Computation and Visualization of Rotational Trajectory Behavior in an Objective Way

Anke Friederici, Holger Theisel, and Tobias Günther

Abstract—Trajectory data consisting of a low number of smooth parametric curves are standard data sets in visualization. For a visual analysis, not only the behavior of the individual trajectories is of interest but also the relation of the trajectories to each other. Moving objects represented by the trajectories may rotate around each other or around a moving center. We present an approach to compute and visually analyze such rotational behavior in an objective way. We introduce trajectory vorticity (TRV), a measure of rotational behavior of a low number of trajectories. We show that it is objective and that it can be introduced in two independent ways: by approaches for unsteadiness minimization and by considering the relative spin tensor. We compare TRV against single-trajectory methods and apply it to a number of constructed and real trajectory data sets, including drifting buoys in the Atlantic, midge swarm tracking data, pedestrian tracking data, pigeon flocks, and a simulated vortex street.

Trajectory data is a standard type of data to be analyzed in visualization. Trajectory data describing the dynamic behavior of moving objects consists of a finite number of 2D or 3D parametric curves where the parameter is usually the time of observation. Trajectory data arises in many application areas. In flow observations, moving objects are tracked over time by sensors, e.g., observational drifters [30] or balloons. In fluid flows, moving objects are observed by particle tracking velocimetry. To observe animal behavior, animals are either equipped with sensors, or their trajectories are observed by optical methods. Examples are trajectories of insect swarms [45] and bird flocks [41]. Trajectories of humans are extracted from crowd simulations or observations [11], [44]. In swarm simulations, individual agents can be tracked. Since moving objects may interact with each other or follow common underlying patterns, a visual analysis should not only focus on representing the paths of individual objects but also show the relation or a common behavior of multiple objects. In general, two kinds of common behavior of moving objects are possible: (1) Hyperbolic (stretching) behavior: the objects may attract or repel each other, or may get attracted or repelled by a common center. In addition, a saddle-like behavior of simultaneous attraction and repelling is possible. (2) Elliptic (rotational) behavior: the objects may rotate around each other or around a (possibly unknown) rotation center/axis. In this paper, we present an approach to visually analyze the rotational behavior of moving objects. We introduce *Trajectory Vorticity* (TRV), the first approach to visually analyze rotational behavior of trajectories in an objective way. Given a (finite and potentially

low) number of trajectories, TRV is a Lagrangian measure indicating whether, and to which degree, objects rotate around each other or a common center.

For TRV, we require objectivity, i.e., independence from the observation frame. While objectivity is a common and obvious demand, it is in fact a rather strong condition, especially when checking the rotation/swirling behavior of moving objects: objective measures should give the same result even under a moving and/or rotating reference frame. In other words, while the inputs will differ when taken from a fixed position, an observer travelling e.g. with one of the moving objects, or under a Euclidean motion, the final output of objective methods must remain the same. In fact, the most challenging part for objective rotation measures is to distinguish between swirling around a common center and a rotating movement of the coordinate system. Imagine the trajectories describe a swarm of birds. Then a static observer outside the swarm should come to the same conclusion about rotational behavior as an observer moving with one of the birds. We consider objectivity as a common and natural requirement for the analysis of a rotational measure.

Given a set of trajectories, we are not only interested in a common rotation of all trajectories but also in finding subsets of trajectories that reveal their own rotational patterns. Given an initial set of trajectories, we search suitable subsets of them revealing a common rotational behavior. It is important to mention that TRV indicates if a set of trajectories reveals a common rotational behavior, and if so, how strong it is. It does not give any information on the reason for the rotation behavior. In this paper, we make the following contributions:

- We introduce a new Lagrangian measure TRV (*trajectory vorticity*), which measures rotational behavior based on at least three trajectories (in 2D) or four trajectories (in 3D), respectively.
- We show that TRV can be derived in two independent ways: by unsteadiness minimization approaches, or by considering the relative spin tensor in a local best-fitting linear time-dependent vector field.
- We prove that TRV is objective.
- We apply the new measure TRV to a number of sparse trajectory data sets, including drifting buoys in the Atlantic, midge tracking data, pedestrian tracking data, pigeon flocks, and trajectories in a simulated vortex street.

I. BASIC CONCEPTS AND RELATED WORK

A. Visualization of trajectory data

Trajectory data can stem from a wide array of sources, with differing degrees of complexity. While we focus on curves in 2D or 3D space without any additional data attached to it, a multitude of visualization methods exists for both higher dimensional spaces as well as multivariate data attached to each sample, see for example He et al. [26]. In low dimensional spaces, a direct spatial mapping is possible through lines or tubes, where additional properties can be encoded by mapping them to color or width [6], [25]. The time aspect of the data can be visualized in different ways. For 2D data, curves can be fully represented in a space-time cube [49], where time is mapped to a third dimension orthogonal to the spatial plane. An example can be seen in Figure 3. A multitude of interactions on such space-time cubes are possible [2], including among others slicing to focus on an individual time frame, as well as collapsing it along the time axis. For more sparse data, collapsing time that way is a valid and simple solution, see for example Figure 5 and 6. When data sets become too dense to focus on individual curves, methods such as heat maps [40], space-time density mapping [7], [27], or visibility optimization [15], [3] may be employed. To assess the expression of multiple fields along trajectories, time activity curves have been used to analyze trends [31], [32].

B. Objectivity

Objectivity, a concept from continuum mechanics, refers to the invariance of a measure under a moving reference system. Let $s(\mathbf{x}, t)$, $\mathbf{w}(\mathbf{x}, t)$, $\mathbf{T}(\mathbf{x}, t)$ be a time-dependent scalar field, vector field and tensor field, respectively. Further, let $\tilde{s}(\tilde{\mathbf{x}}, t)$, $\tilde{\mathbf{w}}(\tilde{\mathbf{x}}, t)$, $\tilde{\mathbf{T}}(\tilde{\mathbf{x}}, t)$ be their observations under the Euclidean frame change

$$\mathbf{x} = \mathbf{Q}(t) \tilde{\mathbf{x}} + \mathbf{b}(t) \quad (1)$$

where $\mathbf{Q} = \mathbf{Q}(t)$ is a time-dependent rotation tensor and $\mathbf{b}(t)$ is a time-dependent translation vector. Then s , \mathbf{w} , \mathbf{T} are *objective* if the following conditions hold, cf. Truesdell and Noll [50]:

$$\tilde{s}(\tilde{\mathbf{x}}, t) = s(\mathbf{x}, t) \quad (2)$$

$$\tilde{\mathbf{w}}(\tilde{\mathbf{x}}, t) = \mathbf{Q}^T \mathbf{w}(\mathbf{x}, t) \quad (3)$$

$$\tilde{\mathbf{T}}(\tilde{\mathbf{x}}, t) = \mathbf{Q}^T \mathbf{T}(\mathbf{x}, t) \mathbf{Q}. \quad (4)$$

Since its introduction to flow analysis [1], objectivity became a common demand for newly-introduced flow measures [19], [5]. In fact, there are a variety of objective flow measures focusing on hyperbolic (stretching) properties, such as FTLE [43]. Also, objective flow measures focusing on elliptic (rotational) behavior have been introduced and can roughly be divided into three classes: (1) *Replacing the spin tensor by the relative spin tensor* [9], [1]: These approaches use the fact that the rate-of-strain-tensor is objective and consider the spin tensor (vorticity) in the local frame given by the eigenbasis of the rate-of-strain tensor. (2) *Replacing the spin tensor by the spin deviation tensor* [23], [29], based on the fact that the difference of two spin tensors at different locations but the same time is objective. (3) *Finding optimal reference frames minimizing the unsteadiness*

of the observed flow: introduced by Günther et al. [14], this created a number of follow-up work [16], [18], [4], [17], [37], [52]. Recently, the objectivity of unsteadiness minimization approaches has been questioned [20] but confirmed [48].

All approaches mentioned above have in common that they rely on an underlying velocity field and its derivatives. For our problem, where only a few trajectories are available, no underlying velocity field exists, and thus, previous approaches are not applicable.

C. Hyperbolic measures for finite sets of trajectories

If the input is not a continuous vector field but only a few trajectories, several methods exist to analyze hyperbolic behavior. *Relative dispersion* (RD) was introduced by Provenzale [36] and further analyzed by Haller and Yuan [24] and Haller [21]. Given are two distinct C^1 continuous n -dimensional ($n = 2, 3$) trajectories $\mathbf{x}_1(t), \mathbf{x}_2(t)$ along with their derivatives $\dot{\mathbf{x}}_1(t), \dot{\mathbf{x}}_2(t)$. Defining the local relative dispersion

$$\text{rd} = \text{rd}_{\mathbf{x}_1(t), \mathbf{x}_2(t)}(t) = \frac{(\mathbf{x}_2 - \mathbf{x}_1)^T (\dot{\mathbf{x}}_2 - \dot{\mathbf{x}}_1)}{(\mathbf{x}_2 - \mathbf{x}_1)^T (\mathbf{x}_2 - \mathbf{x}_1)}, \quad (5)$$

one gets the relative dispersion by integrating rd along trajectories:

$$\text{RD}_{\mathbf{x}_1(t), \mathbf{x}_2(t)}^{t_0, t_N} = \int_{t_0}^{t_N} \text{rd} dt = \ln \frac{|\mathbf{x}_2(t_N) - \mathbf{x}_1(t_N)|}{|\mathbf{x}_2(t_0) - \mathbf{x}_1(t_0)|}. \quad (6)$$

Intuitively, RD observes the change of Euclidean distance of two objects over time. Note that RD is objective [21]. Extending RD to more than two trajectories is straightforward.

Haller et al. [21] introduced measures for stretching based on single trajectories only: the *extended trajectory stretching exponents* TSE and $\overline{\text{TSE}}$. Given is a C^2 continuous trajectory $\mathbf{x}(t)$ for $t \in [t_0, t_N]$ with first and second derivatives $\dot{\mathbf{x}}(t), \ddot{\mathbf{x}}(t)$. Then a local stretching measure can be defined as

$$\text{tse} = \text{tse}_{\mathbf{x}(t)}(t) = \frac{\dot{\mathbf{x}}^T \ddot{\mathbf{x}}}{\dot{\mathbf{x}}^T \dot{\mathbf{x}}} \quad (7)$$

from which the Lagrangian measures TSE and $\overline{\text{TSE}}$ are computed by integrating tse along the trajectory:

$$\text{TSE}_{\mathbf{x}(t)}^{t_0, t_N} = \frac{1}{\Delta t} \int_{t_0}^{t_N} \text{tse} dt = \frac{1}{\Delta t} \ln \frac{|\dot{\mathbf{x}}(t_N)|}{|\dot{\mathbf{x}}(t_0)|} \quad (8)$$

$$\overline{\text{TSE}}_{\mathbf{x}(t)}^{t_0, t_N} = \frac{1}{\Delta t} \int_{t_0}^{t_N} |\text{tse}| dt \approx \frac{1}{\Delta t} \sum_{i=0}^{N-1} \left| \ln \frac{|\dot{\mathbf{x}}(t_{i+1})|}{|\dot{\mathbf{x}}(t_i)|} \right| \quad (9)$$

with $\Delta t = t_N - t_0$. The discretization in Eq. (9) samples $\mathbf{x}(t)$ at $N + 1$ time steps $t_0 < t_1 < \dots < t_N$.

D. Rotational measures for finite sets of trajectories

Haller et al. [21] also introduced a rotational measure that is based on a single trajectory only: the *extended trajectory angular velocity* TRA and $\overline{\text{TRA}}$. For defining TRA, the n -dimensional matrix function

$$\text{tra} = \text{tra}_{\mathbf{x}(t)}(t) = \frac{\dot{\mathbf{x}} \ddot{\mathbf{x}}^T - \ddot{\mathbf{x}} \dot{\mathbf{x}}^T}{\dot{\mathbf{x}}^T \dot{\mathbf{x}}} \quad (10)$$

can be introduced to describe the local angular velocity. \mathbf{tra} is an anti-symmetric matrix, from which one gets the following Lagrangian measures by integration along the trajectory

$$\text{TRA}_{\mathbf{x}(t)}^{t_0, t_N} = \frac{1}{\Delta t} \frac{\sqrt{2}}{2} \left| \int_{t_0}^{t_N} \mathbf{tra} dt \right|_{Fr} \quad (11)$$

$$= \frac{1}{\Delta t} \cos^{-1} \frac{\dot{\mathbf{x}}(t_0)^T \dot{\mathbf{x}}(t_N)}{|\dot{\mathbf{x}}(t_0)| |\dot{\mathbf{x}}(t_N)|} \quad (12)$$

$$\overline{\text{TRA}}_{\mathbf{x}(t)}^{t_0, t_N} = \frac{1}{\Delta t} \frac{\sqrt{2}}{2} \int_{t_0}^{t_N} |\mathbf{tra}|_{Fr} dt \quad (13)$$

$$\approx \frac{1}{\Delta t} \sum_{i=0}^{N-1} \cos^{-1} \frac{\dot{\mathbf{x}}(t_i)^T \dot{\mathbf{x}}(t_{i+1})}{|\dot{\mathbf{x}}(t_i)| |\dot{\mathbf{x}}(t_{i+1})|} \quad (14)$$

where Fr denotes the Frobenius norm of a matrix.

Objectivity of single trajectory methods: Single-trajectory measures like TSE and TRA are attractive because they need minimal information to infer the hyperbolic or rotational behavior. Obviously, single-trajectory measures cannot be objective in the Euclidean observation space because one may think of a reference system moving with the trajectory, making each trajectory zero [21]. Because of this, Haller et al. [21] considered objectivity in an extended phase space along with an approach to non-dimensionalization. Further, [21] introduced the concept of quasi-objectivity: contrary to classical objectivity where a scalar value must be invariant under arbitrary time-dependent Euclidian transformations, for quasi-objectivity a condition (A) is introduced, and invariance is only demanded for those fulfilling (A). In fact, Haller et al. [21] claimed that TSE and $\overline{\text{TSE}}$ are objective in the extended phase space, and that TRA and $\overline{\text{TRA}}$ are quasi-objective in the extended phase space under a certain condition put to the average vorticity in a certain neighborhood of the trajectory. Theisel et al. [46] showed that the claims about objectivity in the extended phase space in [21] are incorrect. As a reaction, in an erratum Haller et al. [22] gave up the idea of considering extended phase space and non-dimensionalization. Instead, a new condition for quasi-objectivity was introduced, and theorems about the quasi-objectivity of TSE and TRA were formulated. By showing a simple counter-example, Theisel et al. [47] claim that the corrected theorems in [22] are still incorrect.

II. TRAJECTORY VORTICITY

In the following, we introduce our new objective measure of rotating object behavior that is based on very few trajectories only, *Trajectory Vorticity* (TRV). The input of TRV is a number of (2D or 3D) trajectories. We begin with describing the main idea of TRV in Section II-A, followed by a formal definition and an algorithm for its computation in Sections II-A–II-D. Section II-E collects properties of the measure, while Section II-F shows that the measure can be computed in an alternative way: by minimizing unsteadiness of a local vector field.

A. Main idea of TRV

In nD space ($n = 2, 3$), we consider m distinct C^2 continuous trajectories $\mathbf{x}_1 = \mathbf{x}_1(t)$, $\mathbf{x}_2 = \mathbf{x}_2(t), \dots, \mathbf{x}_m = \mathbf{x}_m(t)$ for $t \in [t_0, t_N]$. In addition, we consider their first derivatives

$\dot{\mathbf{x}}_1, \dot{\mathbf{x}}_2, \dots, \dot{\mathbf{x}}_m$, and second derivatives $\ddot{\mathbf{x}}_1, \ddot{\mathbf{x}}_2, \dots, \ddot{\mathbf{x}}_m$. Note that we require $m \geq 3$ in 2D and $m \geq 4$ in 3D. We introduce an n -dimensional anti-symmetric time-dependent matrix function

$$\mathbf{trv} = \mathbf{trv}_{\mathbf{x}_1, \dots, \mathbf{x}_m}(t) \quad (15)$$

that describes the strength of the rotational behavior of the trajectories $\mathbf{x}_1, \dots, \mathbf{x}_m$ at the time t : the more rotational behavior the trajectories $\mathbf{x}_1, \dots, \mathbf{x}_m$ exhibit at time t , the larger is $\mathbf{trv}_{\mathbf{x}_1, \dots, \mathbf{x}_m}(t)$.

The trajectories \mathbf{x}_i may contain noise and uncertainty that also influence the computation of \mathbf{trv} . While for some configurations of the trajectories the computation of \mathbf{trv} is stable (i.e., small changes in \mathbf{x}_i result in small changes in \mathbf{trv}), for other configurations we may observe instability, i.e., small changes in \mathbf{x}_i may result in large changes in \mathbf{trv} . Clearly, for a final consideration of rotational behavior, stable information should be preferred over unstable ones. To cope with this, we introduce a non-negative time-dependent scalar function

$$s = s_{\mathbf{x}_1, \dots, \mathbf{x}_m}(t) \quad (16)$$

that denotes the computational stability of \mathbf{trv} at the time t . In fact, s drops to 0 if \mathbf{trv} cannot be computed locally.

Based on \mathbf{trv} and s , we define the Lagrangian Trajectory Vorticity TRV by a weighted integration of \mathbf{trv} as

$$\text{TRV}_{\mathbf{x}_1, \dots, \mathbf{x}_m}^{t_0, t_N} = \frac{\sqrt{2}}{2} \frac{\left| \int_{t_0}^{t_N} s \mathbf{trv} dt \right|_{Fr}}{\int_{t_0}^{t_N} s dt} \quad (17)$$

$$\overline{\text{TRV}}_{\mathbf{x}_1, \dots, \mathbf{x}_m}^{t_0, t_N} = \frac{\sqrt{2}}{2} \frac{\int_{t_0}^{t_N} |s \mathbf{trv}|_{Fr} dt}{\int_{t_0}^{t_N} s dt} \quad (18)$$

with Fr denoting the Frobenius norm of a matrix. The computation of TRV and $\overline{\text{TRV}}$ requires a non-zero denominator in (17) and (18), i.e., the stability s must not vanish everywhere. Note that a locally vanishing s is not a problem as long as it does not vanish over the entire temporal domain. Both (17) and (18) describe a weighted integration of \mathbf{trv} , resulting in a convex combination of the \mathbf{trv} values over time. Thus, not the stability s itself influences the final TRV and $\overline{\text{TRV}}$ but the ratio of s to the average s over the whole temporal domain. In fact, assuming a discretization of (17) similar to (14) gives

$$\text{TRV} = \frac{\sqrt{2}}{2} \left| \sum_{i=0}^N w_i \mathbf{trv}_i \right|_{Fr}, \quad \overline{\text{TRV}} = \frac{\sqrt{2}}{2} \sum_{i=0}^N w_i |\mathbf{trv}_i|_{Fr} \quad (19)$$

with $w_i = \frac{s_i}{\sum_{j=0}^N s_j}$ and $s_i = s \left(\frac{N-i}{N} t_0 + \frac{i}{N} t_N \right)$ and therefore

$$\sum_{i=0}^N w_i = 1. \quad (20)$$

With TRV, clockwise and counterclockwise rotations cancel each other out, while with $\overline{\text{TRV}}$ their norm is accumulated. We offer both since the right choice is application-dependent, e.g., based on noise sensitivity. For trajectories with homogeneous rotation behavior, TRV and $\overline{\text{TRV}}$ give similar results.

In particular, we mention two special cases. If s is constant over time (i.e., $s(t) = s > 0$), Eqs. (17) and (18) simplify to

$$\text{TRV} = \frac{1}{\Delta t} \frac{\sqrt{2}}{2} \left| \int_{t_0}^{t_N} \text{trv} dt \right|_{Fr}, \quad \overline{\text{TRV}} = \frac{1}{\Delta t} \frac{\sqrt{2}}{2} \int_{t_0}^{t_N} |\text{trv}|_{Fr} dt \quad (21)$$

which are independent of s . Further, if trv is constant over time, then Eqs. (17) and (18) simplify to

$$\text{TRV} = \overline{\text{TRV}} = \frac{\sqrt{2}}{2} |\text{trv}|_{Fr}, \quad (22)$$

i.e., TRV and $\overline{\text{TRV}}$ are independent of $s(t)$, as well.

B. Definition of trv

To define the local measure trv , we consider a best-fitting spatially linear time-dependent velocity field

$$\mathbf{v} = \mathbf{v}_{\mathbf{x}_1, \dots, \mathbf{x}_m}(\mathbf{x}, t) = \mathbf{J}_{\mathbf{x}_1, \dots, \mathbf{x}_m}(t) \mathbf{x} + \mathbf{a}_{\mathbf{x}_1, \dots, \mathbf{x}_m}(t) \quad (23)$$

where $\mathbf{J} = \mathbf{J}_{\mathbf{x}_1, \dots, \mathbf{x}_m}(t)$ is a time-dependent Jacobian matrix and $\mathbf{a} = \mathbf{a}_{\mathbf{x}_1, \dots, \mathbf{x}_m}(t)$ is a time-dependent vector. In fact, we search $\mathbf{J}(t), \mathbf{a}(t)$ such that all trajectories $\mathbf{x}_1(t), \dots, \mathbf{x}_m(t)$ are as close as possible to pathlines of \mathbf{v} , i.e., \mathbf{J}, \mathbf{a} solve:

$$\sum_{i=1}^m \|\dot{\mathbf{x}}_i(t) - \mathbf{v}(\mathbf{x}_i, t)\|^2 \rightarrow \min. \quad (24)$$

In fact, for $n = 2$ and $m = 3$, \mathbf{v} can be chosen such that all trajectories are pathlines of \mathbf{v} . The same holds for $n = 3$ and $m = 4$. To obtain an objective measure of rotation, we then follow Drouot and Lucius [9] and Astarita [1] and observe the spin tensor in the frame given by the eigenvectors of the rate-of-strain tensor, which is objective. We obtain the rate-of-strain tensor \mathbf{S} and the spin tensor \mathbf{W} from $\mathbf{J} = \mathbf{S} + \mathbf{W}$ via:

$$\mathbf{S} = \frac{\mathbf{J} + \mathbf{J}^T}{2}, \quad \mathbf{W} = \frac{\mathbf{J} - \mathbf{J}^T}{2}. \quad (25)$$

From this, we consider $\mathbf{E} = \mathbf{E}(t)$ to be the rotation matrix containing the (normalized) eigenvectors of \mathbf{S} as columns, and $\dot{\mathbf{E}} = \dot{\mathbf{E}}(t) = \frac{d\mathbf{E}}{dt}$ is its time-derivative. Removing the strain rotation rate tensor \mathbf{W}_s , which contains the rotation of the chosen eigenvector basis

$$\mathbf{W}_s = -\mathbf{E} \dot{\mathbf{E}}^T, \quad (26)$$

we compute trv as the relative spin tensor \mathbf{W}_r [9], [1] by

$$\text{trv}_{\mathbf{x}_1, \dots, \mathbf{x}_m}(t) = \mathbf{W}_r = \mathbf{W} - \mathbf{W}_s. \quad (27)$$

C. Computation of trv

While Section II-B gives a complete definition of trv , it is not feasible yet for direct computation as its formulation contains a minimizer (24) and the derivative of a rotation matrix (26). In this section, we provide a complete algorithm to compute trv , including explicit solutions of \mathbf{v} and \mathbf{W}_s . For this, we introduce the $((n+1) \times m)$ time-dependent matrices

$$\mathbf{X} = \mathbf{X}(t) = \begin{pmatrix} \mathbf{x}_1 & \mathbf{x}_2 & \dots & \mathbf{x}_m \\ 1 & 1 & \dots & 1 \end{pmatrix} \quad (28)$$

$$\dot{\mathbf{X}} = \dot{\mathbf{X}}(t) = \begin{pmatrix} \dot{\mathbf{x}}_1 & \dot{\mathbf{x}}_2 & \dots & \dot{\mathbf{x}}_m \\ 0 & 0 & \dots & 0 \end{pmatrix} \quad (29)$$

$$\ddot{\mathbf{X}} = \ddot{\mathbf{X}}(t) = \begin{pmatrix} \ddot{\mathbf{x}}_1 & \ddot{\mathbf{x}}_2 & \dots & \ddot{\mathbf{x}}_m \\ 0 & 0 & \dots & 0 \end{pmatrix} \quad (30)$$

which stack the position \mathbf{x}_i , velocity $\dot{\mathbf{x}}_i$, and acceleration $\ddot{\mathbf{x}}_i$ at a specific time t from all considered trajectories. In order to fit a linear vector field in the form of (23), we first compute

$$\mathbf{H} = \mathbf{H}(t) = \dot{\mathbf{X}} \mathbf{X}^{-1}, \quad \dot{\mathbf{H}} = \dot{\mathbf{H}}(t) = (\ddot{\mathbf{X}} - \mathbf{H} \dot{\mathbf{X}}) \mathbf{X}^{-1}. \quad (31)$$

Note that for $m = n+1$ (i.e., \mathbf{X} is a quadratic matrix), \mathbf{X}^{-1} is the usual matrix inverse. For $m > n+1$, \mathbf{X}^{-1} in (31) denotes the *right* Moore-Penrose pseudo-inverse $\mathbf{X}^T (\mathbf{X} \mathbf{X}^T)^{-1}$ instead of the matrix inverse. From (31), we get the best-fitting velocity field in (23) by

$$\begin{pmatrix} \mathbf{J}(t) & \mathbf{a}(t) \\ \mathbf{0}^T & 0 \end{pmatrix} = \mathbf{H}(t), \quad \begin{pmatrix} \dot{\mathbf{J}}(t) & \dot{\mathbf{a}}(t) \\ \mathbf{0}^T & 0 \end{pmatrix} = \dot{\mathbf{H}}(t) \quad (32)$$

with $\dot{\mathbf{J}} = \frac{d\mathbf{J}}{dt}$. From this, strain tensor \mathbf{S} and spin tensor \mathbf{W} are computed by (25), and the strain tensor time derivative $\dot{\mathbf{S}} = \frac{d\mathbf{S}}{dt}$ is computed as

$$\dot{\mathbf{S}} = \frac{\dot{\mathbf{J}} + \dot{\mathbf{J}}^T}{2}. \quad (33)$$

To obtain \mathbf{E} , we compute a matrix factorization of \mathbf{S} by

$$\mathbf{S} = \mathbf{E} \bar{\mathbf{S}} \mathbf{E}^T \quad (34)$$

such that \mathbf{E} is the rotation vector containing the eigenvectors of \mathbf{S} as columns, and $\bar{\mathbf{S}}$ is a diagonal matrix. Having \mathbf{E} , we also transform $\dot{\mathbf{S}}$ into the local reference system given by \mathbf{E} :

$$\bar{\dot{\mathbf{S}}} = \mathbf{E}^T \dot{\mathbf{S}} \mathbf{E}. \quad (35)$$

From this, we obtain the strain rotation tensor in the \mathbf{E} frame:

$$\overline{\mathbf{W}}_s = \begin{pmatrix} 0 & -u_3 & [u_2] \\ u_3 & 0 & [-u_1] \\ [-u_2] & [u_1] & [0] \end{pmatrix} \quad (36)$$

with

$$([u_1, u_2, u_3]) = \left(\left[\frac{\bar{\mathbf{S}}_{3,2}}{\bar{\mathbf{S}}_{2,2} - \bar{\mathbf{S}}_{3,3}}, \frac{\bar{\mathbf{S}}_{1,3}}{\bar{\mathbf{S}}_{3,3} - \bar{\mathbf{S}}_{1,1}} \right], \frac{\bar{\mathbf{S}}_{2,1}}{\bar{\mathbf{S}}_{1,1} - \bar{\mathbf{S}}_{2,2}} \right) \quad (37)$$

where $\bar{\mathbf{S}}_{i,j}$ denotes the entry at $[i, j]$ of the matrix $\bar{\mathbf{S}}$, and $\bar{\dot{\mathbf{S}}}_{i,j}$ denotes the entry at $[i, j]$ of the matrix $\bar{\dot{\mathbf{S}}}$, respectively. (Note that in (36), (37) content in brackets $[]$ refers to additional content present in 3D but not in 2D.) Finally, the back transformation of $\overline{\mathbf{W}}_s$ into the original frame gives

$$\mathbf{W}_s = \mathbf{E} \overline{\mathbf{W}}_s \mathbf{E}^T \quad (38)$$

from which the final trv is computed by (27).

D. Definition and Computation of s

The stability of the computation of trv depends on the stability of the eigenvectors of the rate-of-strain tensor \mathbf{S} because the computation requires a factorization of \mathbf{S} in (34). If small changes in the trajectories \mathbf{x}_i lead to small changes in the eigenvectors of \mathbf{S} , we can expect a stable computation of trv . Since the stability of the eigenvectors of \mathbf{S} depends on the (dis-)similarity of the eigenvalues of \mathbf{S} , we define the stability function s as

$$s = s_{\mathbf{x}_1, \dots, \mathbf{x}_m}(t) = \min(\{|\bar{\mathbf{S}}_{1,1} - \bar{\mathbf{S}}_{2,2}|, [|\bar{\mathbf{S}}_{2,2} - \bar{\mathbf{S}}_{3,3}|, |\bar{\mathbf{S}}_{3,3} - \bar{\mathbf{S}}_{1,1}|]\}) \quad (39)$$

which is the minimum of the denominator(s) in Eq. (37). Note that $\bar{\mathbf{S}}_{1,1}, \bar{\mathbf{S}}_{2,2}, [\bar{\mathbf{S}}_{3,3}]$ are the eigenvalues of \mathbf{S} .

We remark that trv can only be computed if $\mathbf{X}\mathbf{X}^T$ has full rank, see Eq. (31). If $\mathbf{X}\mathbf{X}^T$ has a rank deficit, then $s(t)$ is set to 0, making the computation of trv from Eq. (17)–(18) in this particular time instance obsolete. This case, however, did not occur in any application presented later in the paper.

E. Properties of trv , s , TRV

Lemma 1: \mathbf{W}_s in (26) and (38) are identical.

This lemma tells that the computation of trv in Section II-B corresponds to the definition of trv in Section II-A. To show that for $m = n+1$ (28)–(32) and (23) give a velocity field \mathbf{v} for which $\mathbf{x}_i(t)$ are pathlines, we have to show $\mathbf{v}(\mathbf{x}_i(t), t) = \dot{\mathbf{x}}_i(t)$ for $i = 1, \dots, m$. Using (23), this can be reformulated as

$$\begin{pmatrix} \mathbf{J}(t) & \mathbf{a}(t) \\ \mathbf{0}^T & 0 \end{pmatrix} \begin{pmatrix} \mathbf{x}_i(t) \\ 1 \end{pmatrix} = \begin{pmatrix} \dot{\mathbf{x}}_i(t) \\ 0 \end{pmatrix} \quad (40)$$

with $\mathbf{J}(t)$ denoting the Jacobian matrix and $\mathbf{a}(t)$ a spatially constant vector, see (23). Writing this for all i in a row gives $\mathbf{H}\mathbf{X} = \dot{\mathbf{X}}$ which is equivalent to (31). Further, (34)–(38) is an equivalent formulation to (26).

Theorem 1: $\text{trv}_{\mathbf{x}_1, \dots, \mathbf{x}_m}(t)$ is objective.

The formal proof of this theorem is in the supplementary appendix.

Theorem 2: $s_{\mathbf{x}_1, \dots, \mathbf{x}_m}(t)$ is objective.

This follows directly from the fact that \mathbf{S} is objective. Since the diagonal entries of $\bar{\mathbf{S}}$, namely $\bar{\mathbf{S}}_{1,1}, \bar{\mathbf{S}}_{2,2}$, and $\bar{\mathbf{S}}_{3,3}$, are the eigenvalues of \mathbf{S} , cf. Eq. (34), the diagonal entries of $\bar{\mathbf{S}}$ inherit the objectivity from \mathbf{S} .

From theorems 1 and 2 follows directly that TRV and $\overline{\text{TRV}}$ are objective as well, since they are calculated from $\text{trv}(t)$ and $s(t)$, see Eqs. (17)–(18).

F. An alternative definition of trv

Surprisingly, trv can also be obtained in a different way: by unsteadiness minimization following Günther et al. [14]. Note that \mathbf{v} defined in (23) also has a spatially linear time-derivative

$$\mathbf{v}_t(\mathbf{x}, t) = \dot{\mathbf{J}}(t) \mathbf{x} + \dot{\mathbf{a}}(t). \quad (41)$$

Observing \mathbf{v} defined in (23) in a moving reference frame $\tilde{\mathbf{x}} = \mathbf{R}(t) \mathbf{x} + \mathbf{c}(t)$ gives for the time-derivative of \mathbf{v} in the new reference frame [14]

$$\tilde{\mathbf{v}}_t = \mathbf{R}(\mathbf{v}_t - \mathbf{M}\mathbf{u}) \quad (42)$$

with $\mathbf{M} = (-\mathbf{J}\mathbf{x}_p + \mathbf{v}_p, \mathbf{J}, \mathbf{x}_p, \mathbf{I})$, $\mathbf{x}_p = \begin{pmatrix} 0 & -1 \\ 1 & 0 \end{pmatrix} \mathbf{x}$, $\mathbf{v}_p = \begin{pmatrix} 0 & -1 \\ 1 & 0 \end{pmatrix} \mathbf{v}$ in 2D, and $\mathbf{M} = (-\mathbf{J}\mathbf{X} + \mathbf{V}, \mathbf{J}, \mathbf{X}, \mathbf{I})$, $\mathbf{X} = sk(\mathbf{x})$, $\mathbf{V} = sk(\mathbf{v})$ in 3D, and \mathbf{u} is a 6-vector in 2D and 12-vector in 3D:

$$\mathbf{u} = \begin{pmatrix} \mathbf{u}_1 \\ \mathbf{u}_2 \\ \mathbf{u}_3 \\ \mathbf{u}_4 \end{pmatrix} = \begin{pmatrix} ap(\mathbf{R}^T \dot{\mathbf{R}}) \\ \mathbf{R}^T \dot{\mathbf{c}} \\ ap(\mathbf{R}^T \dot{\mathbf{R}} - (\mathbf{R}^T \dot{\mathbf{R}})^2) \\ -(\mathbf{R}^T \dot{\mathbf{c}} - \mathbf{R}^T \dot{\mathbf{R}} \mathbf{R}^T \dot{\mathbf{c}}) \end{pmatrix} \quad (43)$$

where ap transforms the anti-symmetric part of a matrix to a scalar/vector: $ap(\mathbf{M}) = \frac{1}{2}(\mathbf{M}_{1,2} - \mathbf{M}_{2,1})$ in 2D and $ap(\mathbf{M}) = \frac{1}{2}(\mathbf{M}_{3,2} - \mathbf{M}_{2,3}, \mathbf{M}_{1,3} - \mathbf{M}_{3,1}, \mathbf{M}_{2,1} - \mathbf{M}_{1,2})^T$ in 3D. Conversely, sk is the inverse function transforming a scalar/vector to an anti-symmetric matrix, here for 2D/3D:

$$sk(\alpha) = \begin{pmatrix} 0 & \alpha \\ -\alpha & 0 \end{pmatrix}, \quad sk \begin{pmatrix} \alpha \\ \beta \\ \gamma \end{pmatrix} = \begin{pmatrix} 0 & -\gamma & \beta \\ \gamma & 0 & -\alpha \\ -\beta & \alpha & 0 \end{pmatrix} \quad (44)$$

which is also referred to as skew-symmetric matrix [14]. Note that due to the spatial linearity of \mathbf{v} , both \mathbf{v}_t and $\tilde{\mathbf{v}}_t$ are spatially linear as well. Then, searching for an unsteadiness minimizing observation frame results in searching an unknown \mathbf{u} fulfilling

$$\int_U \|\tilde{\mathbf{v}}_t\|^2 dV \rightarrow \min \quad (45)$$

where U is a certain 2D/3D neighborhood. Note that due to the spatial linearity of \mathbf{v} , the problem in Eq. (45) is under-determined in \mathbf{u} , i.e., it has a whole family of solutions \mathbf{u} . However, all solutions of (45) have the same component \mathbf{u}_1 , that is, component \mathbf{u}_1 is independent of the size and location of U . With this, we get

$$\mathbf{W}_s = -sk(\mathbf{u}_1) \quad (46)$$

The proof of the equivalence of (38) and (46) is a straight computation for which we provide a Maple sheet in the accompanying material. Eq. (46) gives that trv can be computed by observing \mathbf{W} in an unsteadiness minimizing reference frame following Günther et al. [14].

Remarks: The equivalence of unsteadiness minimization and relative spin tensor consideration shown here does not hold for general vector fields but only for spatially linear ones as considered here.

Another popular approach to objectivize flow measures is to replace \mathbf{W} by the spin-deviation tensor [23], [29]

$$\mathbf{W} - \frac{1}{\text{vol}(U)} \int_U \mathbf{W} dV. \quad (47)$$

For \mathbf{v} defined in (23), this gives a perfectly objective but trivial solution: it is zero everywhere.

III. SELECTION OF TRAJECTORY SUBSETS

TRV computes the rotational behavior for a set of trajectories and a fixed time interval. For real trajectory data sets (e.g. tracking of particles in a flow), considering all trajectories simultaneously over the entire integration time usually does not give a relevant result. Thus, strategies are needed to select trajectory subsets and time spans in which TRV is calculated.

A. Choice of trajectories

To compute TRV and $\overline{\text{TRV}}$ for each trajectory in a data set, a number of reference trajectories need to be selected for each trajectory. While it would be possible to always consider the whole trajectory set, this would only reveal macroscopic behavior, while neglecting more localized rotations. Instead, we compute a local TRV and $\overline{\text{TRV}}$ for each available trajectory.

Given is the set of M available trajectories $\{\mathbf{x}_1(t), \dots, \mathbf{x}_M(t)\}$. For each trajectory $\mathbf{x}_j(t)$, we consider

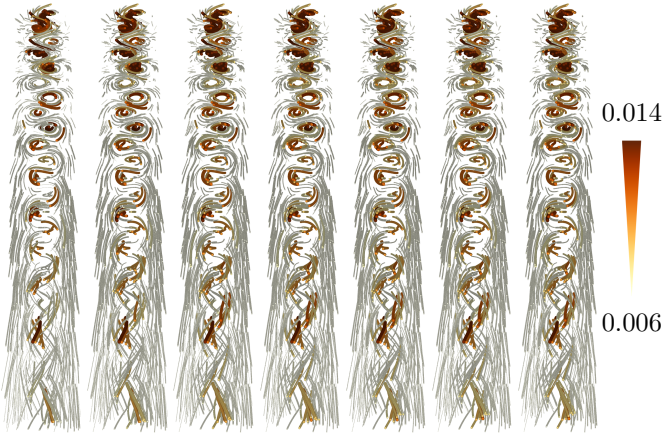


Fig. 1. Automatic selection of m for the CYLINDER dataset. From left to right, the maximum number for the m nearest trajectories is increased, from which the m with highest $\overline{\text{TRV}}$ is chosen ($m \in \{4, 6, \dots, 16\}$). For higher m , the $\overline{\text{TRV}}$ value decreases, which is why results look the same for high m .

the m closest neighboring trajectories $\{\mathbf{x}_{j_1}(t), \dots, \mathbf{x}_{j_m}(t)\}$ for which we compute TRV and $\overline{\text{TRV}}$ as

$$\text{TRV}_j = \text{TRV}_{\mathbf{x}_{j_1}, \dots, \mathbf{x}_{j_m}}^{t_0, t_N}, \quad \overline{\text{TRV}}_j = \overline{\text{TRV}}_{\mathbf{x}_{j_1}, \dots, \mathbf{x}_{j_m}}^{t_0, t_N}. \quad (48)$$

In order to define the closest neighboring trajectories, we define a distance metric between the trajectories, for which we use the integrated, squared L^2 distance:

$$d(\mathbf{x}_1(t), \mathbf{x}_2(t)) = \int_{t_0}^{t_N} \|\mathbf{x}_1(\tau) - \mathbf{x}_2(\tau)\|^2 d\tau. \quad (49)$$

Since the trajectories are in temporal correspondence, more general distance metrics, such as the reduced mean closest point distance [33], are not necessary. We compute TRV and $\overline{\text{TRV}}$ for the m closest trajectories.

User-defined m : The first option is to let the user select the number of trajectories m . We demonstrate and discuss the effect of m on the final result in Section V. Ideally, m should be chosen such that the considered trajectories are part of the same rotating phenomenon. This is not easy to select, since multiple rotating phenomena might be in the data set that are represented with a varying number of trajectories.

Best in range: Another option is to test different m within a range $[m_{min}, m_{max}]$ for each trajectory and to find automatically the m that has the strongest vortical behavior. The lower end of the range m_{min} is determined by the dimensionality, i.e., $m_{min} = 3$ (for 2D) and $m_{min} = 4$ (for 3D). The upper end of the range is user-defined. Different choices for m_{max} are examined in Fig. 1, where the $\overline{\text{TRV}}$ value is mapped to color and line radius. Computationally, all m in the range are easily tested by calculating the distances between trajectories once, and by incrementally adding the next closest trajectory to the columns of the matrices \mathbf{X} , $\tilde{\mathbf{X}}$, $\tilde{\tilde{\mathbf{X}}}$ in Eqs. (28)–(30). It would be imaginable to discard trajectory sets for which the stability s is close to zero over the whole time span, although this has not occurred in our experiments.

B. Choice of time span

While the selection method outlined above works well when the distance between curves remains relatively constant, some

data sets contain trajectories whose closest neighbors vary noticeably over time. In these cases, choosing sets of curves by their average distance over their full time range is not the optimal approach. Similarly, the rotational behavior may not remain constant over time, which is not visible by only showing average values of TRV and $\overline{\text{TRV}}$ per line. To address this problem, we implemented a variant of our method which evaluates TRV and $\overline{\text{TRV}}$ for each time step t of a trajectory instead. Then, trajectories are only considered within a time range $[t - \tau, t + \tau]$, both for the distance calculation in the neighborhood search as well as for the calculation of TRV and $\overline{\text{TRV}}$. The neighbors are again chosen by the distance metric in Eq. (49), and may vary along the line. By repeating the process for each vertex (at its respective time t) along the trajectory, we are able to visualize the rotational behavior over time.

C. TRV versus field reconstruction

For each trajectory \mathbf{x}_j with $j \in \{1, \dots, M\}$, the computation of TRV_j and $\overline{\text{TRV}}_j$ requires the estimation of a best-fitting local linear vector field $\mathbf{v}_j(\mathbf{x}, t) = \mathbf{v}_{\mathbf{x}_{j_1}, \dots, \mathbf{x}_{j_m}}(\mathbf{x}, t)$ see Eq. (23). This means that for the computation of TRV and $\overline{\text{TRV}}$, we need to fit M different linear vector field \mathbf{v}_j , $j \in \{1, \dots, M\}$. While these fields are considered as auxiliary fields for the computation of TRV and $\overline{\text{TRV}}$ only, the question arises if we can use them (or any other information from the trajectories $\mathbf{x}_1, \dots, \mathbf{x}_M$) to reconstruct a global (non-linear) vector field \mathbf{v} .

The reconstruction of a smooth velocity field \mathbf{v} from a number of trajectories is a standard sampling problem for which a variety of solutions exist. For example, Particle tracking velocimetry (PTV) approaches heavily rely on stable reconstruction techniques for \mathbf{v} , all of which require a certain density of the trajectories to allow a stable reconstruction. If this is available and a stable reconstruction is possible, it is not necessary to apply single-trajectory or few-trajectory techniques like TRV because for a reconstructed vector field \mathbf{v} there exist a variety of approaches to analyze rotational behavior in an objective way, see Section I-B. TRV and $\overline{\text{TRV}}$ are explicitly designed for cases where the available trajectories are so sparse that a reconstruction of a smooth underlying vector field is not possible. This also has implications on the visual representation: TRV is not a smooth field but a single value for each trajectory (along with its m closest neighbors). In particular, any interpolation between single TRV values is not allowed due to the sparsity of the samples.

IV. RESULTS

In the following, we apply our approach to a number of data sets. We begin with a synthetic example to demonstrate the capability of our approach to separate rotating motion from reference frame rotation.

A. Three trajectories

We consider a simple data set consisting of three 2D trajectories $\mathbf{x}_1(t)$, $\mathbf{x}_2(t)$, $\mathbf{x}_3(t)$ constructed in the following

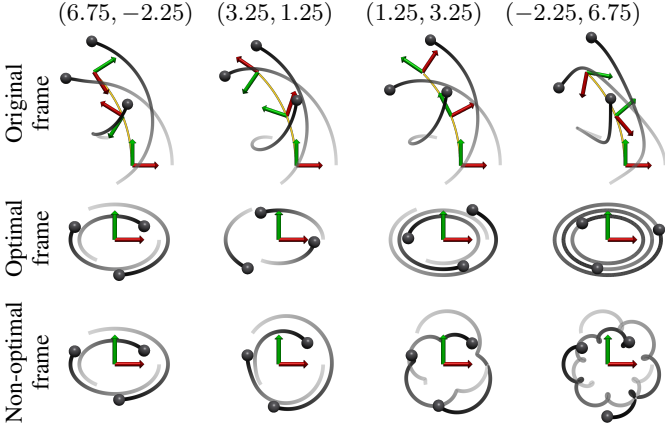


Fig. 2. Example of three trajectories rotating around a point on a circle at different speeds. In the first row, the trajectories and reference frame are shown over $\pi/4$. Removing the respective reference frame gives the second row results, rendered over $\pi/2$: the particles are moving in an ellipse around the origin, their speed and direction depending on the choice of q . Removing the non-optimal reference frame (here from the first line set) leads to non-stationary behavior, shown in the third row.

way: we start with trajectories

$$\mathbf{y}_1(t) = \frac{1}{10} \begin{pmatrix} 3 \cos(qt) \\ 2 \sin(qt) \end{pmatrix} \quad (50)$$

$$\mathbf{y}_2(t) = \frac{2}{25} \begin{pmatrix} 3 \cos\left(qt - \frac{2}{3}\pi\right) \\ 2 \sin\left(qt - \frac{2}{3}\pi\right) \end{pmatrix} \quad (51)$$

$$\mathbf{y}_3(t) = \frac{3}{25} \begin{pmatrix} 3 \cos\left(qt + \frac{2}{3}\pi\right) \\ 2 \sin\left(qt + \frac{2}{3}\pi\right) \end{pmatrix}, \quad (52)$$

each of them describing a rotational movement around the origin with the same angular speed q but different starting points. For each of them, q is a measure of the strength of rotation in the sense that q is proportional to the rotation of the locally fitted velocity field. Hence, we observe how q can be obtained from single or few trajectory diagnostics. We further observe $\mathbf{y}_i(t)$ in a moving reference system (1) resulting in

$$\mathbf{x}_i(t) = \mathbf{Q}(t) \mathbf{y}_i(t) + \mathbf{b}(t) \quad (53)$$

$$\mathbf{b}(t) = \begin{pmatrix} \cos(t) \\ \sin(t) \end{pmatrix}, \quad \mathbf{Q}(t) = \begin{pmatrix} \cos(pt) & -\sin(pt) \\ \sin(pt) & \cos(pt) \end{pmatrix} \quad (54)$$

and $i = 1, 2, 3$. Then the trajectories $\mathbf{x}_i(t)$ are the result of a superposition of two rotational movements: a rotation of the local reference system with angular speed p , and a rotation of particles in this local reference system with angular speed q .

The objectivity of TRV ensures that we can separate the movement of the reference system from the movement of the particles in it. In fact, applying our approach to $\mathbf{x}_1(t)$, $\mathbf{x}_2(t)$, $\mathbf{x}_3(t)$, gives

$$\mathbf{trv} = \begin{pmatrix} 0 & -\frac{13}{12}q \\ \frac{13}{12}q & 0 \end{pmatrix}, \quad s = \frac{5}{6}|q| \quad (55)$$

as shown in the supplemental Maple sheet. Since here, s is independent of t , inserting (55) into (17) and (18) gives

$$\text{TRV} = \overline{\text{TRV}} = \frac{13}{12}|q|. \quad (56)$$

The upper row of Figure 2 shows the motion of the particles in a fixed global reference system as well as the motion of the

TABLE I
LISTING OF TRA, $\overline{\text{TRA}}$, TRV, AND $\overline{\text{TRV}}$ FOR THE THREE TRAJECTORIES DATA SET AND FOUR INSTANCES FOR (p, q) . NOTE THAT $\text{TRV} = \overline{\text{TRV}} = \frac{13}{12}|q|$, WHILE TRA AND $\overline{\text{TRA}}$ VARY FOR THE THREE TRAJECTORIES AND ARE NOT ABLE TO RECOVER q . TRV, AND $\overline{\text{TRV}}$ ARE EQUAL SINCE THE ROTATION DIRECTION DOES NOT CHANGE THE SIGN.

q	-2.25	1.25	3.25	6.75
$\text{TRA}_{\mathbf{x}_1(t)}^{0,2\pi}$	4.000	4.500	4.500	1.500
$\text{TRA}_{\mathbf{x}_2(t)}^{0,2\pi}$	4.256	1.237	1.224	1.201
$\text{TRA}_{\mathbf{x}_3(t)}^{0,2\pi}$	4.625	4.683	4.709	0.750
$\text{TRV}_{\mathbf{x}_1, \mathbf{x}_2, \mathbf{x}_3}^{0,2\pi}$	2.438	1.354	3.521	7.312

q	-2.25	1.25	3.25	6.75
$\overline{\text{TRA}}_{\mathbf{x}_1(t)}^{0,2\pi}$	4.386	4.500	4.500	4.381
$\overline{\text{TRA}}_{\mathbf{x}_2(t)}^{0,2\pi}$	4.275	3.172	3.201	4.021
$\overline{\text{TRA}}_{\mathbf{x}_3(t)}^{0,2\pi}$	4.861	4.683	4.709	4.827
$\overline{\text{TRV}}_{\mathbf{x}_1, \mathbf{x}_2, \mathbf{x}_3}^{0,2\pi}$	2.438	1.354	3.521	7.312

optimal moving reference systems. From the particle motion in the fixed global system it is hard to infer the rotation behavior of the trajectories around each other. This changes when switching to the optimal local moving reference system (middle rows): here we can clearly observe clockwise rotation in the first column and a counterclockwise rotation of different angular speed in the remaining columns. For reference, the lower row shows the observation in the reference frame of the first column, showing a non-stationary particle behavior.

It is unclear if TRA by Haller et al. [21] can be applied to this data set, since [21] formulates conditions about an underlying velocity field which does not exist here. We nevertheless analyze if TRA by Haller et al. [21] can infer the trajectory rotation strength q if the moving observer (in particular p) is unknown. For this, we consider four instances of $\mathbf{x}_i(t)$ by setting $(p, q) = (6.75, -2.25), (3.25, 1.25), (1.25, 3.25), (-2.25, 6.75)$. Note that for all instances we have $p + q = 4.5$, resulting in visually rather similar trajectories $\mathbf{x}_i(t)$ (see the upper row of Figure 2 and the accompanying video), but significantly different rotation strength q .

Table I lists numerical results for TRA (top) and $\overline{\text{TRA}}$ (bottom) using Eqs. (11) and (13) for the three trajectories $\mathbf{x}_i(t)$ (lines of the table) and the four instances (p, q) (columns of the table) at an integration time from 0 to 2π . It shows that neither TRA nor $\overline{\text{TRA}}$ is able to infer q while q directly relates to TRV and $\overline{\text{TRV}}$ by $\text{TRV} = \overline{\text{TRV}} = \frac{13}{12}|q|$.

B. A counter-factual example

To construct a case where our method fails, we modify the three trajectory example from Section IV-A by replacing Eqs. (50)–(52) by

$$\mathbf{y}_1(t) = \frac{1}{4} \begin{pmatrix} \cos(qt) \\ \sin(qt) \end{pmatrix} \quad (57)$$

$$\mathbf{y}_2(t) = \frac{1}{5} \begin{pmatrix} \cos\left(qt - \frac{2}{3}\pi\right) \\ \sin\left(qt - \frac{2}{3}\pi\right) \end{pmatrix} \quad (58)$$

$$\mathbf{y}_3(t) = \frac{3}{10} \begin{pmatrix} \cos\left(qt + \frac{2}{3}\pi\right) \\ \sin\left(qt + \frac{2}{3}\pi\right) \end{pmatrix} \quad (59)$$

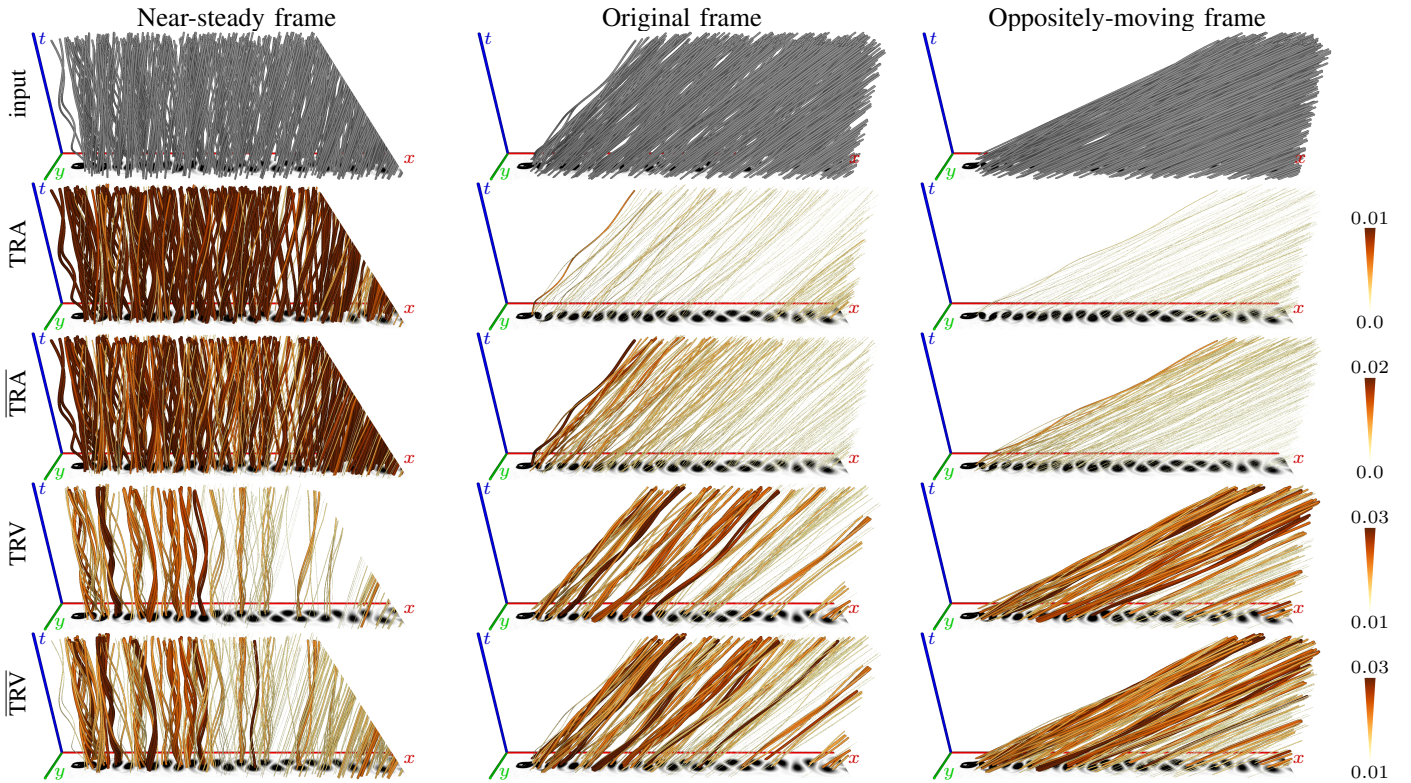


Fig. 3. Trajectory vortex measures calculated from 500 randomly placed pathlines in the CYLINDER flow for three Galilean observers, here shown in 2D space-time. Left to right: an observer moving approximately relative to the vortices, the original observer, and an observer moving in the opposite direction. For reference, vorticity magnitude is visualized in the first time slice. Note that the value of TRA and $\overline{\text{TRA}}$ changes for different observers, while TRV and $\overline{\text{TRV}}$ give consistent results. Pathlines were transformed from the original reference frame via Eq. (1) with $\mathbf{Q}(t) = \mathbf{I}$ and $\mathbf{b}(t) = (\pm 0.9t, 0)^T$ to the near-steady and oppositely-moving frame, respectively. The values of TRA, $\overline{\text{TRA}}$, TRV, and $\overline{\text{TRV}}$ are mapped to both color and line radius.

and keeping (53), (54). This means that the trajectories \mathbf{y}_i move on perfect circles around the origin. Applying TRV to $\mathbf{x}_1, \mathbf{x}_2, \mathbf{x}_3$ gives

$$\mathbf{v} = \begin{pmatrix} 0 & -p-q \\ p+q & 0 \end{pmatrix} \mathbf{x} + (1-p-q) \begin{pmatrix} -\sin(t) \\ \cos(t) \end{pmatrix} \quad (60)$$

and therefore $s = 0$ and trv is undefined. In this example, stability drops to zero everywhere, making it impossible to compute trv because \mathbf{S} does not have distinct eigenvectors. This corresponds to intuition: if \mathbf{y}_i move on perfect circles, one cannot distinguish between particle motion and circular motion of the reference frame, making it impossible to compute rotation in an objective way for this example.

C. Cylinder flow

We apply our approach to the numerically simulated CYLINDER data set, which was simulated using Gerris flow solver [35] and was published by Günther et al. [14]. Such a data set is not the main target of our approach because the underlying velocity field is available here. We use it as a test data set since we can compute an arbitrary number of trajectories and can compare measures based on them with "ground truth" measures from the underlying velocity field.

Figure 3 shows trajectory measures for rotating behavior from 500 randomly seeded trajectories (pathlines) observed in three different reference systems: a system moving with the approximate speed of the vortices (left column), the original

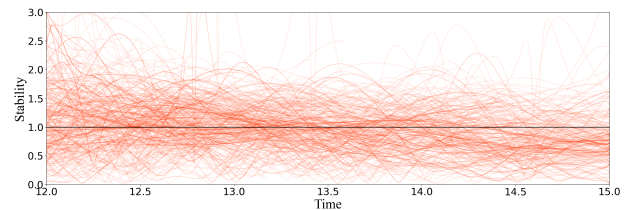


Fig. 4. To protect TRV and $\overline{\text{TRV}}$ from numerical issues, we introduced the stability $s(t)$. Here, a normalized stability $s_n(t) := \frac{s(t)}{\int_{t_0}^{t_N} s(\tau) d\tau} \cdot (t_N - t_0)$ is shown for all trajectories in the CYLINDER flow. If the stability is constant along the trajectory for all $t \in [t_0, t_N]$ then s_n is equal to 1.

references system (middle column), and a system moving in the opposite direction (right column). For reference, we color code the vorticity magnitude of the underlying velocity field in the first time slice, giving a reliable indicator where to expect rotation behavior. Figure 3 illustrates again that TRA and $\overline{\text{TRA}}$ are not objective: corresponding trajectories for different observation frames (columns in Figure 3) have different colors. For TRV and $\overline{\text{TRV}}$, we observe the same colors for different frames, confirming objectivity. We also note that TRV and $\overline{\text{TRV}}$ tend to have high values in regions of high vorticity magnitude, confirming the detection of rotation trajectory behavior. Figure 4 shows that the stability s drops only at a few locations to a small number. In this example, the smallest stability $s(t)$ was $2.2 \cdot 10^{-5}$ and 0.02% of all vertices exhibited a stability below 10^{-4} .

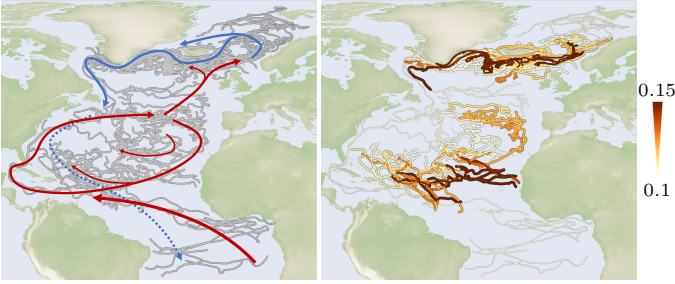


Fig. 5. On the left, input trajectories of drifting buoys in the Atlantic are shown, along with a schematic depiction of the thermohaline currents in the North Atlantic Ocean. Red arrows denote the generalized paths of warm, salty surface water, notably the North Atlantic Gyre, feeding the North Atlantic Current, which eventually cool off enough to form the North Atlantic Deep Water (blue). On the right, our new trajectory vortex measure $\overline{\text{TRV}}$ is visualized for $m = 4$. It reveals the Greenland Current, a cold stream carrying melt water from the Arctic southwards through a region of strong vorticity, through rotational particle behavior. The $\overline{\text{TRV}}$ value is mapped to color and line radius.

D. Ocean drifter trajectories

One instrument for measuring oceanic flow is drifting buoys, which get released into the ocean and are tracked by satellites. The result is a time series per buoy encompassing their position, speed, and potentially other measurements from equipment attached to the drifters. More than a thousand such drifters are currently deployed by the National Oceanic and Atmospheric Administration (NOAA) of the USA, with tracking data freely available [30]. Drifter trajectories have often been employed to track mesoscale eddies, from simple geometric methods identifying "loopers" [39] to techniques relying on statistical [51] or oscillatory [28] analyses. While not objective, these methods work well due to their use of geophysical properties.

We applied our $\overline{\text{TRV}}$ measure with (49) and 3 nearest neighbors per curve on a subset of 126 drifters in the North Atlantic ocean, tracked from Oct 2, 2019 to Sep 13, 2020. Our method allows us to identify regions of highly vortical behavior in an objective manner. The results are shown in Figure 5: while both mesoscale eddies and oceanic gyres are structures of interest to the oceanographic community and prevalent in this region of the data [42], the sparsity of trajectories in these regions does not allow their detection. Instead, strong rotational behavior can be seen in and around the Greenland Current. While not turbulent itself, the current is bounded by bands of high absolute vorticity and is thus picked up as a feature of interest by our measure. When combined with specialized knowledge from the oceanographic community, we believe that $\overline{\text{TRV}}$ can lead to further insight into oceanic eddy phenomena.

E. Midge trajectories

We analyze trajectories of tracked swarms of *Chironomus riparius*. The data set is described and provided by Sinhuber et al. [45]. *Chironomus riparius* are a midge species that consistently and predictably forms mating swarms [8]. Males are known to nucleate over visual features on the ground, such as tree stumps or stream banks [8]. In the experiment, this was simulated by adding "swarm markers" to the setup. The tracking was done by an optical 3-camera system at 100Hz.



Fig. 6. $\overline{\text{TRV}}$ calculated for two different seeding times in the measured MIDGE data set. For this 3D data set, m is selected automatically in $m \in \{4, 6\}$ locally for each point within a time range of 3s using a prior curve smoothing with $\lambda = 10$, see Eq. (61). The total number of input trajectories in the data sets are 38 (left) and 56 (right).

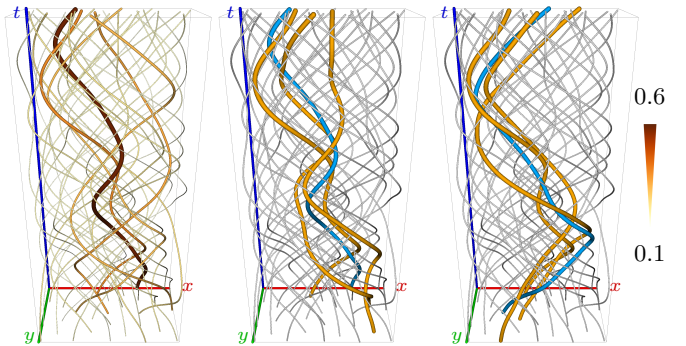


Fig. 7. Left: $\overline{\text{TRV}}$ on space-time tracks of PEDESTRIANS (starting from the bottom) with automatic m selection in $m \in \{3, \dots, 10\}$. Middle and right: three closest trajectories (orange) of a selected trajectory (blue) on which the $\overline{\text{TRV}}$ value was computed.

We apply $\overline{\text{TRV}}$ to further analyze the movement around visual features. In particular, we analyze if a common objective rotation behavior can be observed. Figure 6 shows the trajectories for two different seeding times. While the pure shape of the trajectories does not reveal any patterns, we found a few trajectories with high $\overline{\text{TRV}}$ values, mostly in the inner parts of the data set. Our approach can confirm a swirling behavior of a few trajectories, while the majority of the midges do not exhibit objective rotation behavior.

F. Pedestrians

In an effort to study the walking patterns of pedestrians during the COVID-19 pandemic, Echeverría-Huarte et al. [11] tracked the movement of 18 to 32 pedestrians in a confined space. Test subjects were told to keep a minimum safety distance to each other while walking at a constant speed either randomly or intermittently towards the walls. Based on their trajectories, they found a prevalence of counter-clockwise vortical movement [12].

We applied $\overline{\text{TRV}}$ on one of these data sets and were able to confirm the presence of objective vortical motion at least by a few of the participants, shown both in Figure 7 and the accompanying video. Figure 7 (left) shows $\overline{\text{TRV}}$ on the trajectories, highlighting five trajectories with increased rotation rate. Interestingly, these trajectories are not rotating around each other. This can be seen in Figure 7 (middle and right), where for a selected trajectory (blue) the three closest trajectories

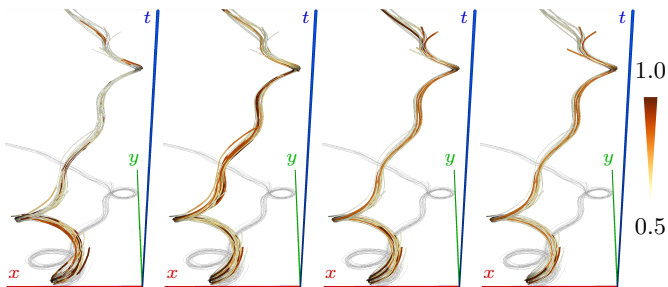


Fig. 8. Space-time tracks of PIGEONS (starting at the bottom) during pursuit by a robot falcon. From left to right, variations of the time window are shown over which $\overline{\text{TRV}}$ with $m = 4$ was calculated, namely 0.2s, 1s, 2s, 3s.

(orange) are shown that were used in the computation of $\overline{\text{TRV}}$. Overall, we can conclude that the counter-clockwise rotational movement observed by the authors [12] depends on the chosen constant reference frame and would mostly disappear in our objectively chosen reference frame and is therefore not objective.

G. Pigeon flock

As another example, we look into the flight paths of birds evading a predator. In this data set, homing pigeons evade a remotely controlled robotic peregrine falcon [41], [34]. Their trajectories are tracked horizontally via GPS and sometimes cut short by invalid position values received. We show the $\overline{\text{TRV}}$ values computed on the 21st experimental run in Figure 8, with a large flock of 34 birds fleeing from the predator. After being released, the flock performs coordinated turns to escape.

To analyze the flocking behavior over time, we calculate the $\overline{\text{TRV}}$ value for each time step separately, as discussed in Section III. Varying the sampled time range highlights different aspects of the data: When taking each data point by itself (left), we can compare the rotational behavior of the birds along their path. Immediately after their release from the cage, the birds perform a collective turn to evade the robot falcon, while assembling into a flock. This is highlighted by relatively high $\overline{\text{TRV}}$ values during the first 5 seconds, where a lot of re-ordering and thus rotation around each other occurs. At the second evasive maneuver, we can observe that while performing a much tighter loop the flock's flight pattern is rather stable and objective rotations occurs only sporadically and briefly, even as the flock as a whole performs a turn. This matches well with the findings in Sankey et al. [41] that show a high level of alignment broken only when a predator comes close. With an increased time range, the values are smoothed along the lines. This highlights how most of the birds do not exhibit any rotation relative to the flock, with three outliers highlighted due to their high trajectory vorticity.

H. Boids simulation

At its basic level, the formation of these kinds of bird flocks can be modelled by a simple set of rules observed by each bird-oid individual, or *boi*d [38]. Cohesion towards the center of mass, alignment with neighboring boids and separation to avoid collision can together closely mimic real-life swarms.

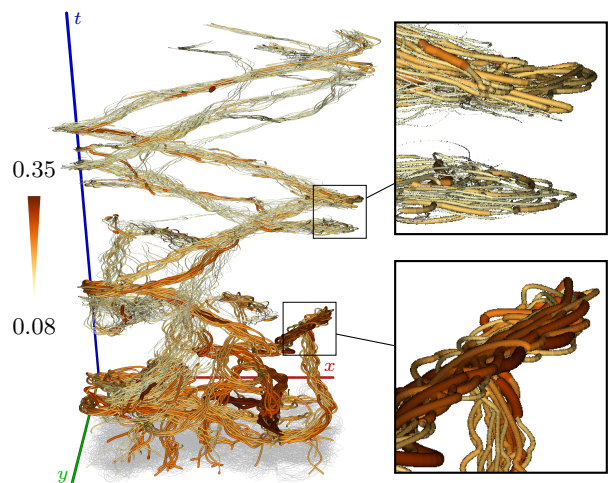


Fig. 9. Space-time tracks (starting from the bottom) of the BOIDS simulation for $m = 5$. During the initial chaotic phase, the agents rotate around each other as they slowly form clusters (bottom right). After some time, the agents arrange into larger flocks and stop rotating almost entirely (top right).

Rotation is not described directly by a rule of the system, but its emergence can be observed in the vorticity of the resulting paths. We recorded the trajectories of 100 boids from an open source implementation [10]. The full space-time data is shown in Figure 9 and the accompanying video. Starting from random positions, $\overline{\text{TRV}}$ values are high everywhere while the agents' movements appear chaotic. Clusters quickly form and the boids begin to align, ceasing to rotate around each other. After some time, only a few big swarms remain, with only the occasional agent showing objective rotational behavior. In this example, motion is a superposition of multiple components (rotation, separation, chaotic motion). Our rotation-only measure is able to detect behavioral differences.

V. DISCUSSION AND LIMITATIONS

Since the input to TRV and $\overline{\text{TRV}}$ is a finite (low) number of trajectories, the quality of the results depends on the input trajectories. A phenomenon can only be observed when a sufficient number of trajectories participate in it and are considered neighbors. We analyze how the results depend on their density, and how TRV and $\overline{\text{TRV}}$ behave if the input is too large (i.e., trajectories far away from each other, showing a different behavior driven by different phenomena). We do the analysis on the cylinder data set where an underlying velocity field as "ground truth" is available. Figure 10 shows the result for different amounts of input trajectories (rows) and different sample sizes (columns). For a low number of input trajectories, sampling many lines tends to include more lines from different regions. This results in fewer high $\overline{\text{TRV}}$ values (Figure 10 upper right). This confirms a desired behavior: too large inputs with more than one dominant motion lead to low $\overline{\text{TRV}}$ values as the dominant motion within a larger region is evaluated instead of smaller-scale phenomena. On the other hand, a larger number of input trajectories (lower row) gives a more stable estimation of the rotating motion. This choice of k , i.e., the number of neighbors sampled, is thus dependent on both the data and scale of the feature in question and should

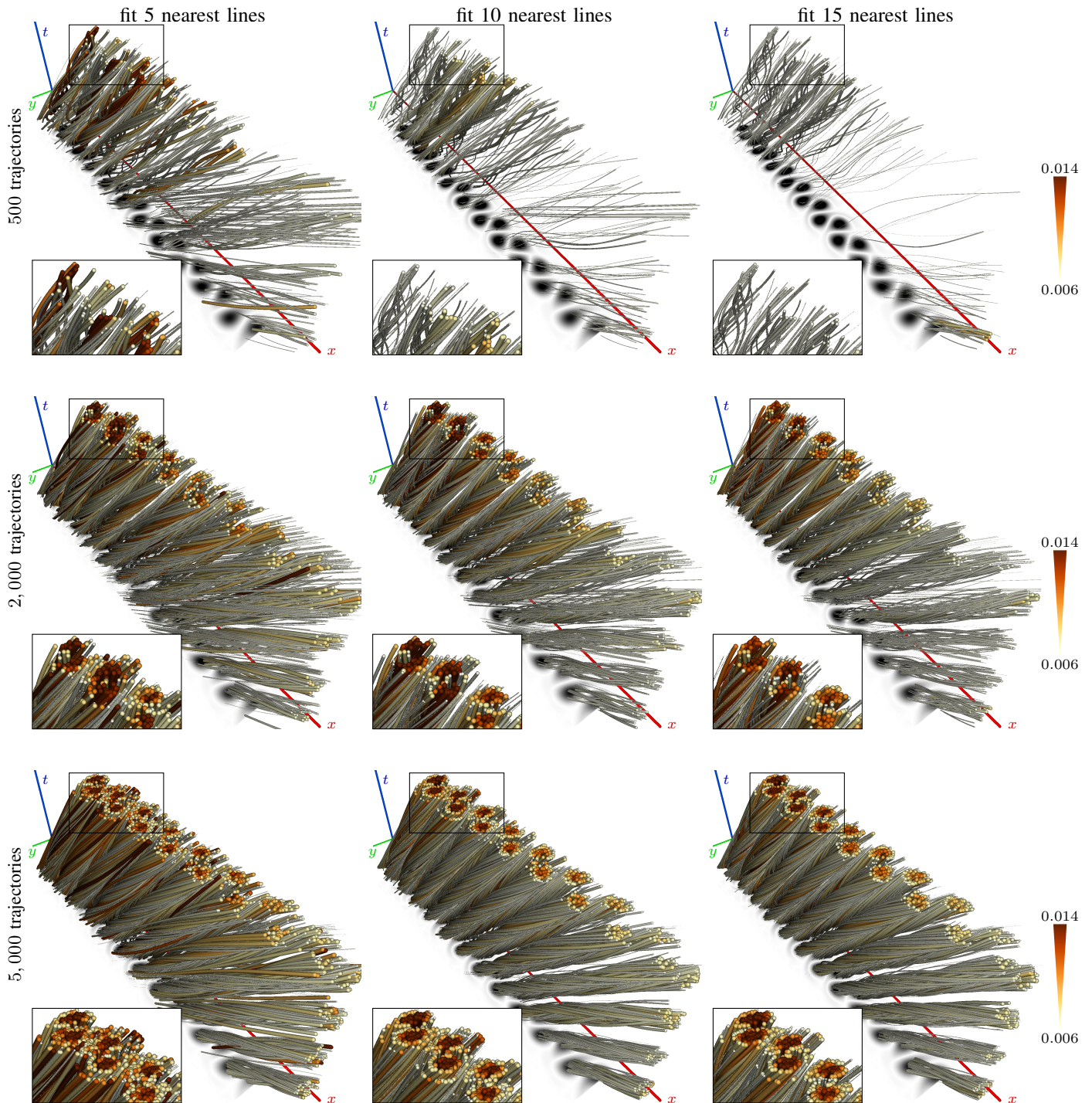


Fig. 10. Parameter studies for the number of input trajectories (rows) and the number of neighboring lines used for fitting \mathbf{H} (columns), here for $\overline{\text{TRV}}$. For a low number of input trajectories (top row), adding too many neighbors includes lines that might not be part of a vortex. For a large number of input trajectories (bottom row), more neighboring lines result in a more stable estimation of rotating motion. Note that with increasing number of input trajectories, vortices are estimated more accurately, as the continuous field is sampled more densely. For reference, the vorticity of the underlying field is shown in grayscale for the bottom slice.

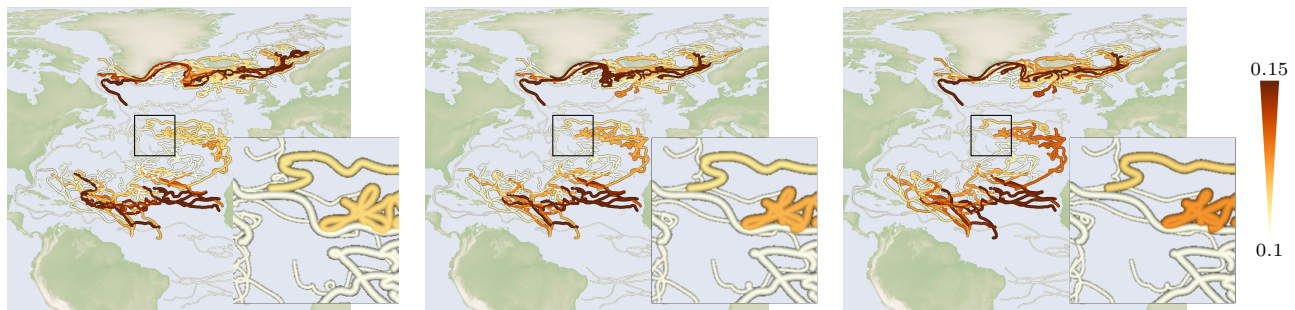


Fig. 11. Before computing line derivatives numerically, we apply a linear smoothing according to Eq. (61), for which different smoothing weights are demonstrated here, from left to right: $\lambda = 1$, $\lambda = 2$, $\lambda = 3$. Increasing the smoothing weights results in smoother line geometry. The TRV observations, however, remain consistent for different parameter choices.

Data set	dist. (ms)	$\overline{\text{TRV}}$ (ms)	lines	vertices	fit
DRIFTER	26.41	161.98	203	125,472	4
MIDGE	0.17	8.81	38	1,558	3
MIDGE	0.36	15.19	56	2,728	3
CYLINDER	25.93	162.54	500	115,241	5
CYLINDER	25.99	184.01	500	112,014	10
CYLINDER	27.49	229.90	500	109,815	15
CYLINDER	354.35	482.14	2,000	471,906	5
CYLINDER	357.94	571.12	2,000	462,457	10
CYLINDER	360.12	758.48	2,000	455,018	15
CYLINDER	1,945.26	1,204.98	5,000	1,199,686	5
CYLINDER	1,930.10	1,440.55	5,000	1,183,928	10
CYLINDER	1,933.80	1,948.60	5,000	1,171,023	15
PEDESTR.	3.60	49.52	18	2,214	3-10
PIGEON 0.2S	500.83	220.51	34	3,498	4
PIGEON 1.0S	1,758.03	922.35	34	3,498	4
PIGEON 2.0S	3,148.76	2,395.13	34	3,498	4
PIGEON 3.0S	3,186.95	2,834.82	34	3,498	4
BOIDS	$1.08 \cdot 10^6$	100,440	100	100,000	5

TABLE II

RUN-TIME MEASUREMENTS FOR THE COMPUTATION OF DISTANCES (IN MILLISEC.), THE $\overline{\text{TRV}}$ COMPUTATION (IN MILLISEC.), THE NUMBER OF TRAJECTORIES, THE TOTAL NUMBER OF VERTICES IN THE SET, AND THE NUMBER OF NEIGHBORING LINES USED (OR CONSIDERED) FOR THE FIT.

ultimately be steerable by the user. Further, $\overline{\text{TRV}}$ needs to be shown on multiple trajectories to detect the extent of the coherently rotating region. Since the data sets covered different phenomena, we did not attempt normalization of the $\overline{\text{TRV}}$ value range. This might be a worthwhile direction to investigate when studying rotating motion of the same phenomenon, for example to compare simulations with experimental measurements.

Table II lists performance measurements for all considered data sets, computed on an Intel Core i9-10980XE CPU with 3.00 GHz. For the real-world data, computations were in the order of milliseconds, while the largest test sets took in total about 4 or 6 seconds, respectively, to compute $\overline{\text{TRV}}$ for all trajectories. The BOIDS simulation took the longest, due to the temporally localized computation of $\overline{\text{TRV}}$ for each vertex. In the non-localized implementation, we compute the full distance matrix between all trajectories first. Afterwards, the distance matrix is reused when finding the k -nearest trajectories for each of the curves, by iterating the corresponding row in the distance matrix and collecting the k smallest items in a max heap. To calculate the tangents and accelerations numerically, we use a sixth-order accurate finite-difference scheme [13].

TRV indicates a common rotational movement of moving objects. TRV, however, is unable to show why this behavior is present. Rotation can have various reasons, depending on the application. If e.g. the trajectories are mass-less particles in a

flow, they follow the underlying Navier-Stokes equations, and rotational behavior indicates a vortical region. For other kinds of trajectories (e.g., swarms of birds), the emergence of vortical behavior is often observed and confirmed by simulations, but there are still ongoing debates about its cause [12], [44], [34].

A. Continuity of the trajectories

The computation of TRV requires (at least piecewise) C^2 trajectories. While this is in general a safe model assumption (for example, a flow fulfilling the Navier-Stokes equation is assumed to be C^∞ continuous), it may create numerical issues in the discretization: second derivatives of trajectories are usually estimated from sampling points on the trajectories, resulting in a dependency of the results from the sampling quality/density. A common approach to get reliable derivatives is smoothing, for which we employed a linear optimization that minimizes the following quadratic energy:

$$\operatorname{argmin}_{\tilde{\mathbf{x}}} \int_{t_0}^{t_N} \frac{1}{2} \|\tilde{\mathbf{x}} - \mathbf{x}\|^2 + \frac{\lambda}{2} \|\dot{\tilde{\mathbf{x}}}\|^2 dt \quad (61)$$

We have analyzed the quality of TRV for various smoothing weights λ in Fig. 11.

VI. CONCLUSION

We have introduced Trajectory Vorticity (TRV), the – to the best of our knowledge – first approach to analyze rotation behavior based on only few trajectories in an objective way. We proved objectivity of TRV and showed that TRV can be carried over from two independent established objectivization methods for velocity field data. Our algorithm was demonstrated on a wide range of data sets, encompassing measured, simulated and integrated trajectories.

VII. SUPPLEMENTARY MATERIAL

The accompanying Maple sheet contains the Maple proof that Eqs. (38), (26), and (46) are equivalent. Further, it contains a Maple proof that the 3 trajectories in (53), (54) have a closed-form solution for trv written in (55).

A. Acknowledgments

This work was supported by DFG grant no. GU 945/3-1 and a scholarship from the German National Academic Foundation.

REFERENCES

- [1] G. Astarita. Objective and generally applicable criteria for flow classification. *Journal of Non-Newtonian Fluid Mechanics*, 6(1):69–76, 1979. doi: 10.1016/0377-0257(79)87004-4
- [2] B. Bach, P. Dragicevic, D. Archambault, C. Hurter, and S. Carpendale. A descriptive framework for temporal data visualizations based on generalized space-time cubes. *Computer Graphics Forum*, 36(6):36–61, 2017. doi: 10.1111/cgf.12804
- [3] I. Baeza Rojo, M. Gross, and T. Günther. Fourier opacity optimization for scalable exploration. *IEEE Transactions on Visualization and Computer Graphics*, 26(11):3204–3216, 2020. doi: 10.1109/TVCG.2019.2915222
- [4] I. Baeza Rojo and T. Günther. Vector field topology of time-dependent flows in a steady reference frame. *IEEE Transactions on Visualization and Computer Graphics*, 26(1):280–290, 2020. doi: 10.1109/TVCG.2019.2934375
- [5] R. Bujack, L. Yan, I. Hotz, C. Garth, and B. Wang. State of the art in time-dependent flow topology: Interpreting physical meaningfulness through mathematical properties. *Computer Graphics Forum*, 39(3):811–835, 2020. doi: 10.1111/cgf.14037
- [6] S. Buschmann, M. Trapp, and J. Döllner. Animated visualization of spatial-temporal trajectory data for air-traffic analysis. *The Visual Computer*, 32:371–381, 2016. doi: 10.1007/s00371-015-1185-9
- [7] U. Demšar and K. Virrantaus. Space-time density of trajectories: exploring spatio-temporal patterns in movement data. *International Journal of Geographical Information Science*, 24(10):1527–1542, 2010. doi: 10.1080/13658816.2010.511223
- [8] A. Downe and V. Caspary. The swarming behaviour of chironomid riparius (diptera: Chironomidae) in the laboratory. *Can. Entomol.*, 105:165–171, 1973. doi: 10.4039/Ent105165-1
- [9] R. Drouot and M. Lucius. Approximation du second ordre de la loi de comportement des fluides simples. Lois classiques déduites de l’introduction d’un nouveau tenseur objectif. *Archivum Mechaniki Stosowanej*, 28(2):189–198, 1976.
- [10] B. Eater. Boids implementation. <https://eater.net/boids/>, 2020.
- [11] I. Echeverría-Huarte, A. Garcimartín, R. Hidalgo, C. Martín-Gómez, and I. Zuriguel. Estimating density limits for walking pedestrians keeping a safe interpersonal distancing. *Scientific reports*, 11(1):1–8, 2021. doi: 10.1038/s41598-020-79454-0
- [12] I. Echeverría-Huarte, A. Nicolas, R. C. Hidalgo, A. Garcimartín, and I. Zuriguel. Spontaneous emergence of counterclockwise vortex motion in assemblies of pedestrians roaming within an enclosure. *Scientific reports*, 12(1):2647, 2022. doi: 10.1038/s41598-022-06493-0
- [13] B. Fornberg. Generation of finite difference formulas on arbitrarily spaced grids. *Mathematics of computation*, 51(184):699–706, 1988.
- [14] T. Günther, M. Gross, and H. Theisel. Generic objective vortices for flow visualization. *ACM Transactions on Graphics (Proc. SIGGRAPH)*, 36(4):141:1–141:11, 2017. doi: 10.1145/3072959.3073684
- [15] T. Günther, C. Rössl, and H. Theisel. Opacity optimization for 3d line fields. *ACM Transactions on Graphics (SIGGRAPH)*, 32(4):120:1–120:8, 2013. doi: 10.1145/2461912.2461930
- [16] T. Günther and H. Theisel. Objective vortex corelines of finite-sized objects in fluid flows. *IEEE Transactions on Visualization and Computer Graphics (Proc. IEEE Scientific Visualization 2018)*, 25(1):956–966, 2019. doi: 10.1109/TVCG.2018.2864828
- [17] T. Günther and H. Theisel. Hyper-objective vortices. *IEEE Transactions on Visualization and Computer Graphics*, 26(3):1532–1547, 2020. doi: 10.1109/TVCG.2018.2868760
- [18] M. Hadwiger, M. Mlejnek, T. Theußl, and P. Rautek. Time-dependent flow seen through approximate observer killing fields. *IEEE Transactions on Visualization and Computer Graphics*, 25(1):1257–1266, 2019. doi: 10.1109/TVCG.2018.2864839
- [19] G. Haller. An objective definition of a vortex. *Journal of Fluid Mechanics*, 525:1–26, 2005. doi: 10.1017/S0022112004002526
- [20] G. Haller. Can vortex criteria be objectivized? *Journal of Fluid Mechanics*, 508:A25, 2021. doi: 10.1017/jfm.2020.937
- [21] G. Haller, N. Aksamit, and A. P. Encinas Bartos. Quasi-objective coherent structure diagnostics from single trajectories. *Chaos: An Interdisciplinary Journal of Nonlinear Science*, 31(4):043131, 2021. doi: 10.1063/5.0044151
- [22] G. Haller, N. Aksamit, and A. P. Encinas Bartos. Erratum: “Quasi-objective coherent structure diagnostics from single trajectories” [Chaos 31, 043131 (2021)]. *Chaos: An Interdisciplinary Journal of Nonlinear Science*, 32(5):059901, 2022. doi: 10.1063/5.0090124
- [23] G. Haller, A. Hadjighasem, M. Farazmand, and F. Huhn. Defining coherent vortices objectively from the vorticity. *Journal of Fluid Mechanics*, 795:136–173, 2016. doi: 10.1017/jfm.2016.151
- [24] G. Haller and G. Yuan. Lagrangian coherent structures and mixing in two-dimensional turbulence. *Phys. D*, 147(3/4):352–370, Dec. 2000. doi: 10.1016/S0167-2789(00)00142-1
- [25] M. Han, I. Wald, W. Usher, Q. Wu, F. Wang, V. Pascucci, C. D. Hansen, and C. R. Johnson. Ray tracing generalized tube primitives: Method and applications. *Computer Graphics Forum*, 38(3):467–478, 2019. doi: 10.1111/cgf.13703
- [26] J. He, H. Chen, Y. Chen, X. Tang, and Y. Zou. Diverse visualization techniques and methods of moving-object-trajectory data: A review. *ISPRS International Journal of Geo-Information*, 8(2), 2019. doi: 10.3390/ijgi8020063
- [27] A. Kuhn, N. Lindow, T. Günther, A. Wiebel, H. Theisel, and H.-C. Hege. Trajectory density projection for vector field visualization. In *Eurographics Conference on Visualization Short Papers*, pp. 31–35. Eurographics, Leipzig, Germany, 2013. doi: 10.2312/PE.EuroVisShort.EuroVisShort2013.031-035
- [28] J. M. Lilly and P. Pérez-Brunius. Extracting statistically significant eddy signals from large Lagrangian datasets using wavelet ridge analysis, with application to the gulf of mexico. *Nonlinear Processes in Geophysics*, 28(2):181–212, 2021. doi: 10.5194/npg-28-181-2021
- [29] J. Liu, Y. Gao, and C. Liu. An objective version of the vortex vector for vortex identification. *Physics of Fluids*, 31(6):065112, 2019. doi: 10.1063/1.5095624
- [30] R. Lumpkin and L. Centurioni. NOAA Global Drifter Program quality-controlled 6-hour interpolated data from ocean surface drifting buoys, subset from 2019-06-30 to 2021-06-30, 2019, accessed 2021-11-15. doi: 10.25921/7ntx-z961
- [31] D. B. Nguyen, L. Zhang, R. S. Laramée, D. Thompson, R. O. Monico, and G. Chen. Unsteady flow visualization via physics based pathline exploration. In *2019 IEEE Visualization Conference (VIS)*, pp. 286–290. IEEE, 2019. doi: 10.1109/VISUAL.2019.8933578
- [32] D. B. Nguyen, L. Zhang, R. S. Laramée, D. Thompson, R. O. Monico, and G. Chen. Physics-based pathline clustering and exploration. *Computer Graphics Forum*, 40(1):22–37, 2021. doi: 10.1111/cgf.14093
- [33] S. Oeltze, D. J. Lehmann, A. Kuhn, G. Janiga, H. Theisel, and B. Preim. Blood flow clustering and applications in virtual stenting of intracranial aneurysms. *IEEE Transactions on Visualization and Computer Graphics*, 20(5):686–701, 2014. doi: 10.1109/TVCG.2013.2297914
- [34] M. Papadopoulos, H. Hildenbrandt, D. W. Sankey, S. J. Portugal, and C. K. Hemelrijk. Emergence of splits and collective turns in pigeon flocks under predation. *Royal Society Open Science*, 9(2):211898, 2022.
- [35] S. Popinet. Free computational fluid dynamics. *ClusterWorld*, 2(6), 2004.
- [36] A. Provenzale. Transport by coherent barotropic vortices. *Annual Review of Fluid Mechanics*, 31:55–93, 1999. doi: 10.1146/annurev.fluid.31.1.55
- [37] P. Rautek, M. Mlejnek, J. Beyer, J. Troidl, H. Pfister, T. Theußl, and M. Hadwiger. Objective observer-relative flow visualization in curved spaces for unsteady 2D geophysical flows. *IEEE Transactions on Visualization and Computer Graphics*, 27(2):283–293, 2021. doi: 10.1109/TVCG.2020.3030454
- [38] C. W. Reynolds. Flocks, herds and schools: A distributed behavioral model. In *Proceedings of the 14th annual conference on Computer graphics and interactive techniques*, pp. 25–34, 1987. doi: 10.1145/37401.37406
- [39] P. Richardson. A census of eddies observed in North Atlantic SOFAR float data. *Progress in Oceanography*, 31(1):1–50, 1993. doi: 10.1016/0079-6611(93)90022-6
- [40] D. Rothlisberger, O. Nierstrasz, S. Ducasse, D. Pollet, and R. Robbes. Supporting task-oriented navigation in IDEs with configurable heatmaps. In *2009 IEEE 17th International Conference on Program Comprehension*, pp. 253–257. IEEE, 2009. doi: 10.1109/ICPC.2009.5090052
- [41] D. W. Sankey, R. F. Storms, R. J. Musters, T. W. Russell, C. K. Hemelrijk, and S. J. Portugal. Absence of “selfish herd” dynamics in bird flocks under threat. *Current Biology*, 31(14):3192–3198, 2021. doi: 10.1016/j.cub.2021.05.009
- [42] W. J. Schmitz Jr and M. S. McCartney. On the north Atlantic circulation. *Reviews of Geophysics*, 31(1):29–49, 1993. doi: 10.1029/92RG02583
- [43] S. C. Shadden, F. Lekien, and J. E. Marsden. Definition and properties of Lagrangian coherent structures from finite-time Lyapunov exponents in two-dimensional aperiodic flows. *Physica D: Nonlinear Phenomena*, 212(3):271–304, 2005. doi: 10.1016/j.physd.2005.10.007
- [44] J. L. Silverberg, M. Bierbaum, J. P. Sethna, and I. Cohen. Collective motion of humans in mosh and circle pits at heavy metal concerts. *Physical review letters*, 110(22):228701, 2013. doi: 10.1103/PhysRevLett.110.228701
- [45] M. Sinhuber, K. Van Der Vaart, R. Ni, J. G. Puckett, D. H. Kelley, and N. T. Ouellette. Three-dimensional time-resolved trajectories from

laboratory insect swarms. *Scientific Data*, 6(1):1–8, 2019. doi: 10.1038/sdata.2019.36

- [46] H. Theisel, A. Friederici, and T. Günther. Objective flow measures based on few trajectories, 2022. doi: 10.48550/ARXIV.2202.09566
- [47] H. Theisel, A. Friederici, and T. Günther. On the objectivity and quasi-objectivity of TSE and TRA. *ArXiv e-prints*, 2023. doi: 10.48550/arXiv.2304.00089
- [48] H. Theisel, M. Hadwiger, P. Rautek, T. Theußl, and T. Günther. Vortex criteria can be objectivized by unsteadiness minimization. *Physics of Fluids*, 33(10):107115, 2021. doi: 10.1063/5.0063817
- [49] H. Torsten. What about people in regional science? *Papers of the Regional Science Association*, 24(1):6–21, 1970. doi: 10.1007/BF01936872
- [50] C. Truesdell and W. Noll. *The Nonlinear Field Theories of Mechanics*. Springer, 1965. doi: 10.1007/978-3-662-10388-3_1
- [51] M. Veneziani, A. Griffa, A. M. Reynolds, Z. D. Garraffo, and E. P. Chassignet. Parameterization of Lagrangian spin statistics and particle dispersion in the presence of coherent vortices. *Journal of Marine Research*, 63:1057–1083, 2005b. doi: 10.1357/002224005775247571
- [52] X. Zhang, M. Hadwiger, T. Theußl, and P. Rautek. Interactive exploration of physically-observable objective vortices in unsteady 2D flow. *IEEE Transactions on Visualization and Computer Graphics*, 28(2):281–290, 2022. doi: 10.1109/TVCG.2021.3115565



Anke Friederici is a PhD student at the Otto-von-Guericke Universität Magdeburg, Germany. Her research interests include flow visualization and topology. Contact her at anke@isg.cs.uni-magdeburg.de.



Holger Theisel is professor for Visual Computing at University of Magdeburg, Germany. In 1994, he received the diploma in Computer Science, in 1996 a Ph.D. in Computer Science, and a habilitation (*venia legendi*) in 2001 from the University of Rostock. His research interests focus on flow visualization as well as on CAGD, geometry processing and information visualization. Contact him at theisel@ovgu.de



Tobias Günther is a professor of computer science at the Friedrich-Alexander-Universität Erlangen-Nürnberg, Germany. His research interests include visualization and physically-based rendering. He received his PhD in scientific visualization from the University of Magdeburg in 2016. Contact him at tobias.guenther@fau.de.